Comparison of energy losses in a 9kW Vanadium Redox Flow Battery

Andrea Trovò, Francesco Picano, Massimo Guarnieri

Department of Industrial Engineering – University of Padua
Interdepartmental Centre Giorgio Levi Cases for Energy Economics and Technology – University of Padua
Via Gradenigo 6/A, 35131 Padova Italy

Abstract. An analysis is presented of the losses occurring in a kW-class vanadium redox flow battery due to species crossover, shunt current, hydraulic pressure drops and pumping, in addition to cell overpotentials. The study was developed on a 9 kW / 27 kW h test facility that includes a stack consisting of a 40 600-cm^2 cells and two 550 L electrolyte tanks. The analysis was carried out combining experimental data and model results. The losses were evaluated as functions of the solutions flow rates at stack currents of 30 A, 50 A and 70 A. Charge-discharge cycles performed at a constant flow factor equal to 8 and thus at variable flow rate were analyzed. Results show that shunt currents have a tenfold to twentyfold higher effect than hydraulic pressure drop inside the stack. As regards cell membranes, it has been found that, in terms of efficiency, the ion conductivity (i.e. cell overpotentials) counts more than species diffusivity (i.e. crossover). Moreover, it was found that pumps and their motors can affect significantly the efficiency of a kW-class vanadium redox flow battery system.

Key words: Vanadium redox flow battery, species crossover, shunt currents, energy losses, pumping losses, efficiency.

1.Introduction

Among energy storage technologies, vanadium redox flow batteries (VRFBs) are receiving increased attention for large-scale applications. The main expectations of this technology are related to its independent sizing of power and energy capacity, long service life, low levelized cost of energy (LCE), low environmental impact, and good energy efficiency [1–4].

Since the last decade, research on VRFBs has intensified with the aim that the this kind of battery gain widespread diffusion worldwide [5]. Several studies concern new cell materials. Advanced electrodes [6,7] and their treatments [8], are developed as well as new membranes [9–11] capable of improved performance. New electrolyte compositions are sought in order to achieve stable high-energy density capacity [12–14]. In addition, a lot of research is carried out on the internal design of VRFB cells, but few studies are reported on the engineering system aspects of large VRFB systems [15].

A number of effects impact on the performance a VRFB stack, such as shunt currents and hydraulic losses. The formers are caused by the different cell electric potentials which drive the vanadium charged species to move along the hydraulic flow paths inside the cells and stack, resulting in electric currents (dubbed “shunt”) and the related Joule losses [16]. The latter are due to the friction losses in the porous electrodes, in the stack

hydraulic paths and in the external hydraulic piping. In addition, losses are also due to the hydraulic ancillary devices, to the cell electrochemical overpotentials and to self-discharge effects resulting from vanadium species crossover through the membranes [17]. Shunt-currents and hydraulic losses can be kept low with a proper hydraulic circuit design, even if they call for opposite choices. In fact, the trade-off between shunt current and pumping losses is the crucial issue in designing VRFB hydraulic circuits [18–21]. High electrolyte flow rates reduce the concentration overpotentials, resulting in improved electric performance [22], but reduce the system efficiency due to higher hydraulic losses. Some studies analyzed the pressure drops and pumping powers at varying electrolyte flow rates in the hydraulic circuits [23–25], but they did not analyze the origin of these losses and how each cause affects the system efficiency.

Several studies on shunt currents have been published. Some models have been developed to assess their effects on the VRFB operation [26,27]. In particular the effect of shunt currents on the coulombic efficiency has been investigated by Yong-Song et al. in [28] and by Fink and Remy in [29]. The former paper suggests to limit the number of cells in the stack below 20 in order to keep shunt current negligible. The latter paper highlights that the inner cells discharge faster than the outer due to shunt currents and suggests to enlarge the cell active area in order to reduce the relative effect of shunt currents on the coulombic efficiency. The authors of the present paper have analyzed how shunt currents may affect the thermal behavior of a VRFB, in both load [30] and stand-by conditions when pumps are turned off [16]. These papers show the non-uniform heating of the cells inside the stack due to shunt currents and how critical temperatures can be reached in the case of heavy-duty operations. The shunt currents arising from different layouts of the hydraulic and electric connections between multiple stacks have been determined and compared by Wandschneider et al. [31] and [32]. They highlight how shunt currents affect the efficiency of multi-stack VFRB systems. A simple evaluation of the losses caused by shunt currents in a 2.5 kW/15 kWh VRFB was presented by Tang et al. [33]: they found that in no-load condition at SOC = 50%, 76% of the heat generated inside the stack were due to the side reactions deriving from electrolyte crossover. The combined effects of shunt currents and hydraulic losses were analyzed by Ye et al. [18], for stacks having different number of cells and also for a battery consisting of several stacks. They conclude that long and narrow pipes are preferable in order to minimize shunt current losses.

Very few papers provide a comparative analysis considering other types of losses in addition to hydraulic and shunt currents terms in multicell stacks. Zhang et al. [34] presented a hydraulic and electric equivalent circuit of a 1kW/1kWh VRFB focused to the computation of the stack electrical performance and pump power consumption. Their model adopted some simplifying assumptions and was supported by a partial experimental validation based on data provided by Kim et al. [35]. At the best of our knowledge, studies which take into account in detail all major losses and which are experimentally validated on a kW-class system are missing in the literature.

This problem is faced in the present paper, that analyses the major losses occurring during charge/discharge cycles in a kW/class VRFB system, which are due to: cell overpotentials, shunt currents, vanadium species

crossover in the membranes, hydraulic pressure drops in the stack, hydraulic pressure drops in the piping and ancillary devices (pumps, motors and their inverters). The aim of the study was to assess their relative contribution to the overall losses and thus their effects of the VRFB system efficiency (SE), in order to identify the key factors to address the design of future high-efficiency systems based on compact stacks.

The investigation was developed on an kW-class VRFB test facility, dubbed "industrial scale" VRFB (IS-VRFB), that is fully instrumented for laboratory purposes and is described in Section 2. Some loss contributions used in the analyses were obtained from experimental data taken on the test facility, while others were evaluated by means of numerical models, validated on IS-VRFB. These models were used to evaluate shunt currents, vanadium species crossover, hydraulic pressure drops in the piping and are described in Section 3. Model validations are discussed in Section 4. Section 5 presents the comparative analysis of the loss contributions and the efficiency assessment in charge/discharge cycles.

Nomenclature

Full symbols	Quantity / parameter	unit
A	membrane area	cm^2
A_k	cross-sectional area in the k-th direction / of k-th element	cm^2
C	vanadium concentration	mol L^{-1}
d	membrane thickness	µm
D	pipe diameter	mm
E_0	open circuit voltage (*OCV*)	V
E_a	activation energy of electrolyte diffusivity	J mol^{-1}
EE	energy efficiency	
F	Faraday constant = 96485 C mol^{-1}	C mol^{-1}
f	friction factor	–
i	electric current	A
j	vanadium ions index	–
K	universal gas constant = 8.314 J $K^{-1}mol^{-1}$	J $K^{-1}mol^{-1}$
k	diffusivity coefficient of electrolyte in membrane	cm^2 min^{-1}
l	length	m
M	electrolyte moles diffusing in the membrane	mol
N	number of cells	–
P	power	W
Q	mass flow rate	L min^{-1}
R	electric resistance	Ω
Re	Reynolds number	–
RTE	round-trip efficiency	%
SE	system efficiency	%
SOC	state of charge	%
t	time	s

T	temperature	K
u	electrolyte speed	m s^{-1}
v	voltage	V
V_c	cell volume	L
W	energy	W h
z	number of electrons in the electrochemical reaction	–
ΔG	Gibbs free energy change	J mol^{-1}
Greek		
α	electrolyte flow factor	–
Δp	pressure difference	bar
ζ	minor loss coefficient	–
η	efficiency	%
μ	electrolyte dynamic viscosity	kg $m^{-1}s^{-1}$
ρ	electrolyte density	kg m^{-3}
σ	electrical conductivity	S m^{-1}
τ	time duration	s, h
Subscripts		
–	negative electrolyte	
+	positive electrolyte	
an	ancillary	
c	cell	
ch	charge	
cn	concentrated (or localized hydraulic losses)	
co	crossover	
dc	discharge	
di	distributed (hydraulic losses)	
h	hydraulic	
i	internal (related to cell overpotentials)	
in	inverter	
j	vanadium ion index	
k	electric circuit index	
m	manifold	
mod	model	
mo	motor	
n	cell index	
pi	piping	
pu	pump	
rt	round trip	
sa	sulfuric acid	

sc	shunt current losses	
s	stack (hydraulic)	
st	standard	
w	wattmeter	
x	sum index	

2. IS-VRFB test facility

2.1 IS-VRFB facility description

IS-VRFB is the kW-class test facility whose performance, parameters and measurements were used in the present analyses [36]. Its stack consists of 40 cells provided with 600-cm^2 cross-sectional area and flow-through electrolyte distribution in 5.7-mm thick porous carbon felt electrodes (Beijing Great Wall) separated by Nafion 212® membranes. The stack has been tested at currents as high as 400 A (i.e. at current densities as high as 665 mA cm^{-2} [37]). The facility presents an open frame structure with the stack positioned above the two electrolyte solution tanks. The layout of the electrolyte piping is show in Fig.1, together with the 3D representation of the whole plant. Two centrifugal pumps (PMD 641) provide the electrolyte flows. Their 120-W three-phase motors are fed at variable frequency in the range 10–50 Hz by means of two static inverters, in order to control the electrolyte flow rates Q, in the range from 3.0 L min^{-1} to 29.5 L min^{-1} (corresponding to a specific flow rate range 2.1–20.5·10^{-3} cm s^{-1}) at 50 Hz.

The study made use of electric and fluid-dynamic experimental data extracted from the measurements available on the IS-VRFB test facility. Stack voltage and current were provided by a voltage probe (LEM CV 3-100/SP3) and two current probes (HAS 50-S and HAS 200-S by LEM), respectively. The positive and negative electrolyte flow rates were given by two electromagnetic flow meters (Proline Promag by Endress+Hauser) and the pressure drops of the positive and negative electrolytes inside the stack was measured with two differential pressure gauges (Deltabar PMD by Endress+Hauser). The power supplied from the grid to the inverters which feed the pumps was measured with a digital wattmeter (Seneca Z203-1). Details on these probes, including measurement ranges and accuracies, are reported in [36]. The IS-VRFB battery management system (BMS) consists of a desktop computer with a LabVIEW environment and of a multichannel interface built around a compact DAQ device (National Instruments). This BMS acquires and processes all probe signals and controls the experiment operations as usually performed in a VRFB system [38,39]. In particular, it controls the pump inverters by means of proportional-integrative-derivative (PID) numerical controllers feed-back driven by the analog voltage signals generated by the flow meters, thus allowing to implement any desired flow rate profiles.

A Power Management System (PMS, Fig.1) controls the electric power flowing into/out of the stack during charge and discharge. This PMS consists of a bidirectional static converter (Dana) with a rated current of ±75

A and a rated voltage of 85 V, which is remotely controlled by the BMS both in potentiostatic or galvanostatic mode, namely as a voltage source or a current source.

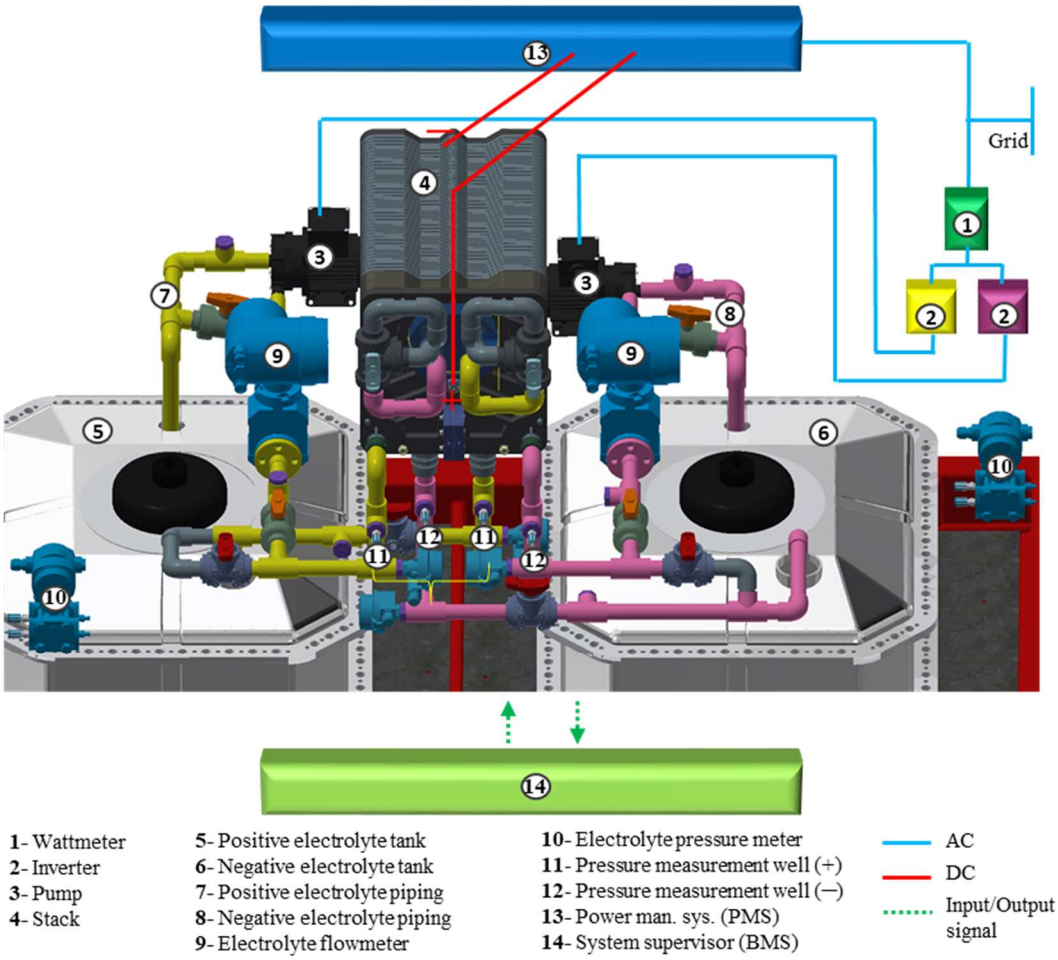

Fig. 1. 3D representation of the IS-VRFB test facility with details of the hydraulic circuit.

2.2 Energy calculations

The study was based on evaluating and comparing the works (energies) converted and/or lost during battery charge and discharge, which were computed by integrating over time the pertinent powers, given by either measurements or numerical models:

$$W = \int_{\tau_{ch,dc}} P dt \tag{1}$$

Numerical integration was performed by the Newton-Cote midpoint rule as $W = \Delta t \, \Sigma_x P_x$, at time steps of $\Delta t = 0.8$ s equal to the sampling time of the BMS, that is four orders of magnitude smaller than the integration interval, i.e. the charge/discharge durations τ_{ch} and τ_{dc} which ranged from about 2 to 10 hours, thus making negligible the numerical integration error. The Newton-Cote midpoints consisted of single measurements performed in steady-state conditions, thus avoiding electric and hydraulic dynamic effect.

The electrical power converted in the stack to develop the energies W_{ch} charged into and W_{dc} discharged from the electrolyte solutions was obtained by multiplying the measured stack voltage v and current i: $P = v\,i$.

The total hydraulic pressure drop in each hydraulic circuit $\Delta p_{h\pm} = \Delta p_{s\pm} + \Delta p_{pi\pm}$ (+ and – indicate the positive and negative electrolyte circuits, respectively) was determined as the sum of a term $\Delta p_{s\pm}$ in the stack and a term $\Delta p_{pi\pm}$ in the piping connecting the stack to the tanks. Notably, $\Delta p_{s\pm}$ were mainly due the porous felts constituting the electrodes whereas the stack manifolds and channels were responsible for much lower contributions. The total hydraulic pressure drops $\Delta p_{h\pm}$ are equated by the pump heads, in order to circulate the electrolytes at flow rates $Q_{\pm}$, so that the total hydraulic power that must be provided by the two pumps, equating the hydraulic losses, are:

$$\begin{aligned} P_{h+} &= Q_{+}\Delta p_{h+} = Q_{+}\left(\Delta p_{s+} + \Delta p_{pi+}\right) = P_{s+} + P_{pi+} \\ P_{h-} &= Q_{-}\Delta p_{h-} = Q_{-}\left(\Delta p_{s-} + \Delta p_{pi-}\right) = P_{s-} + P_{pi-} \end{aligned} \tag{2}$$

In order to compute these expressions, $Q_{\pm}$ and $\Delta p_{s\pm}$ were obtained from measurements provided by the flow meters and from the stack pressure drop gauges in each hydraulic circuit, thus avoiding the need of a detailed model of the hydraulic circuit inside the stack. On the other hand, no measurement of the pressure drops $\Delta p_{pi\pm}$ in the piping connecting the stack to the tanks were available, so that $\Delta p_{pi\pm}$ were determined by means of the hydraulic model presented in Section 3.1. The total power hydraulic losses P_w supplied by the ac grid and measured by the facility ad-hoc wattmeter were affected by the additional losses $P_{an\pm}$ in ancillary devices, namely pump impellers, electric motors and inverters (Fig. 2). These losses were accounted for by means of the efficiencies of the pump impeller $\eta_{pu\pm}$, of the electric motors η_{mo} and of the inverters η_{in}:

$$P_w = \left(P_{h+} + P_{an+}\right) + \left(P_{h-} + P_{an-}\right) = \frac{P_{h+}}{\eta_{in}\,\eta_{mo}\,\eta_{pu+}} + \frac{P_{h-}}{\eta_{in}\,\eta_{mo}\,\eta_{pu-}} \tag{3}$$

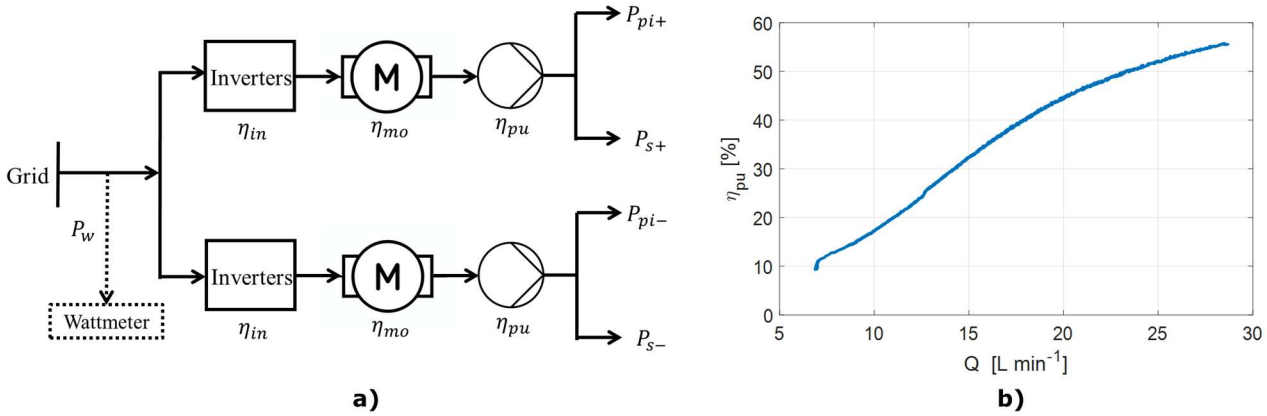

Fig. 2. a) Ancillary power losses composition; b) Pump efficiency η_{pu} vs. flow rate Q of vanadium solution, computed by resolving eq. (3) in terms of η_{pu}. In order to obtain this diagram, the same flow rates were imposed in the positive and negative hydraulic circuits.

The inverter efficiency η_{in} = 95% was obtained from the device data sheet and was assumed constant in every working condition and a bench test on a very similar small three-phase motor gave an efficiency η_{mo} = 50% that was also considered constant in all operations at variable frequency produced by the inverters. Since no efficiency or losses data of the pumps were provided by the manufacturer, η_{pu} was evaluated from eq. (3) as $\eta_{pu\pm} = (P_{h+} + P_{h-}) / P_w \eta_{in} \eta_{mo}$, where: $(P_{h+} + P_{h-})$ was computed according to eq. (2), P_w was measured by means of the wattmeter and η_{in} and η_{mo} were given the aforementioned values. The resulting efficiency η_{pu} as function of Q is shown in Fig 2b and conforms typical centrifugal pump behaviors [40]. By using the above efficiency values, the power losses in the inverter, pump motors and pump impellers in any operating condition were computed as $P_{in} = (1-\eta_{in}) P_w$, $P_{mo} = (1-\eta_{mo}) \eta_{in} P_w$ and $P_{pu} = (1- \eta_{pu}) \eta_{mo} \eta_{in} P_w$, respectively.

3. Numerical models

Numerical models were used to compute the energy losses not available from measurements, namely the losses related to: a) hydraulic pressure drops in the piping, b) shunt currents, c) cell overpotentials, and d) vanadium species crossover in the membranes. Cell-resolved dynamic models of the IS-VRFB system were used at this aim.

3.1 Hydraulic model

A standard hydraulic analytical model was used to compute the electrolyte pressure drop $\Delta p_{pi\pm}$ in the piping as functions of the flow rates $Q_{\pm}$, for the positive and negative electrolyte hydraulic circuits [18], [34], [41,42]. Each electrolyte piping pressure drop was computed as the sum a distributed term $\Delta p_{di\pm}$ due to friction in the straight pipes, and a concentrated (i.e. localized) term $\Delta p_{cn\pm}$ occurring in local components, e.g. elbows, junctions, T-joints, flow meters and valves: $\Delta p_{pi\pm} = \Delta p_{di\pm} + \Delta p_{cn\pm}$. The first term was computed as:

$$\Delta p_{di\pm} = \frac{\rho}{2} \sum_x f_x \frac{l_x}{D_x} u_x^2 \tag{4}$$

where ρ is the fluid density and l_x, D_x and u_x are the pipe length, pipe diameter and fluid velocity in the x-th straight segment, respectively. The pipe friction factor f_x depends on the pipe roughness and on the Reynolds number $Re = \rho u_x D_x / \mu$, with μ the dynamic viscosity, which allows to identify a laminar ($Re < 2300$) or turbulent ($Re > 2300$) flow regime in the pipes. The fluid density ρ and dynamic viscosity μ needed to compute Re were determined experimentally for both electrolytes at SOC = 50%. The measurements were performed with a 1637/02 U-tube reverse flow BS/IP viscometers (Cannon-Fenske) and a pycnometer (Thomas Scientific) and provided the results reported in Tab. 1. These values were assumed constant in the model, as an average during the charge/discharge cycles (i.e. at varying SOC). Consequently, considering that the pipes have smooth internal surfaces, the following expressions were used for f_x [42]:

$$f = \begin{cases} 64 / R & Re < 2300 \\ \left[-1.8 log\left(6.9 / Re\right)\right]^{-2} & Re > 2300 \end{cases} \tag{5}$$

The so-called concentrated (i.e. localized) pressure drops were computed as:

$$\Delta p_{cn\pm} = \frac{\rho}{2} \sum_x \zeta_x u_x^2 \tag{6}$$

where ζ_x are empirical "minor loss" coefficients whose values were obtained from the literature [42] or from the manufacturer's data sheet [43] and are reported in Tab. 1.

Tab. 1: Values of the empirical minor loss coefficient ζ used in calculating the concentrated pressure losses.

Component		**Number in each circuit**	ζ	**Reference**
elbows, 90°		3	1.5	[42]
T-joints, 180° flow		5	0.9	[42]
T-joints, 90° flow		5	2.0	[42]
joints		2	0.08	[42]
pipe inlet (tank outlet)		1	0.8	[42]
pipe outlet (tank inlet)		1	1	[42]
flow meter	inlet (contraction)	1	0.38	[42]
	outlet (expansion)	1	0.48	[42]
valves		2	0.42	[43]

3.2 Shunt current model

In the stack, the cells are connected in series while each manifold segment feds in parallel the cell flow frames and electrodes with the same polarity, which are at different electric potentials. In the loops thus formed electric current flow which are dubbed "shunt currents" and cause Joule losses. A number of methods have been published and patents have been registered for reducing shunt currents. However, analyzing them of the scope of our study, and we assumed the shunt current effect as a loss term to be accounted for. To this aim, a model was developed, based on an equivalent electrical circuit [16]. In this model, each cell was represented as an ideal voltage source $E_{i,n}$ in series with an internal resistance $R_{i,n}$, which represents the cell overpotential voltage drop, both parameters being *SOC* dependent [44]. The electrolyte flow segments of the stack, i.e. manifolds, flow channels and felts, were modeled as resistors [45], as exemplified in the two-cell electric scheme of Fig. 3.

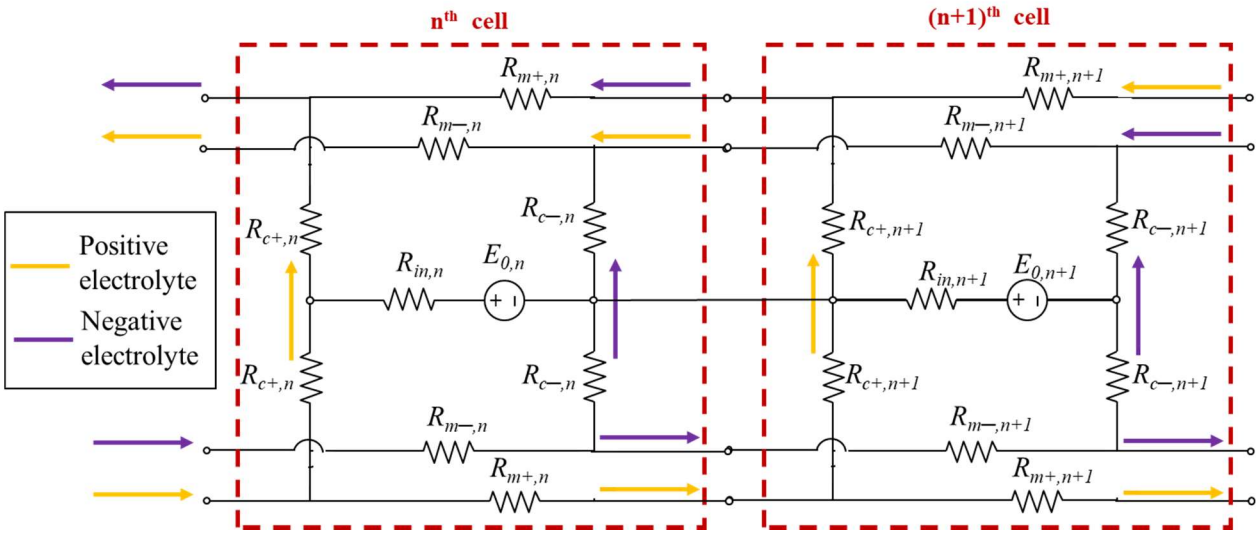

Fig. 3. Stack equivalent electric model for shunt current calculation – exemplification for two consecutive cells.

The resistance of the n-th segment with length $l_{k,n}$ and cross section $A_{k,n}$ was computed as $R_{k\pm,n} = l_{k,n}/\sigma_{k\pm,n} A_{k,n}$, where k stands for manifold (m) and cell flow channel and felts (c). The dependence of the electric conductivity $\sigma_{k\pm,n}$ on the vanadium species concentrations was accounted for by means of the state of charge (SOC) of positive + and negative – electrolyte in each cell:

$$\sigma_+ = SOC_{n+}\sigma_V + (1 - SOC_{n+})\sigma_{IV} \qquad \sigma_- = SOC_{n-}\sigma_{II} + (1 - SOC_{n-})\sigma_{III} \tag{7}$$

where $n = 1 \ldots N$ is the cell index and σ_j are the conductivities of species V_j (with $j = II$, III, IV, V). The numerical solution of the equivalent electric circuit yielded the shunt current $i_{k\pm,n}$ in each segment, from which the pertinent power losses was computed as $P_{k\pm,n} = R_{k\pm,n}\, i_{k\pm,n}^2$ [16]. Summing up all the contributions of the manifolds and cell flow channels and felts, the overall shunt-current power losses were obtained. Similarly, the cell internal power losses associated with the overpotentials were computed as $P_{i,n} = R_{i,n}\, i_{i,,n}^2$. The complete description and validation of the shunt current model is provided in [30] and [16], where detailed representations of the shunt current distributions are provided.

3.3 Species crossover model

The cell membrane has the function of separating the positive and the negative half-cells while allowing hydrogen ions to pass thorough during charge and discharge [45]. However, as a side effect, also the vanadium species permeate through the membrane, thus affecting the overall performance [11]. These permeations were modelled by means of the first Fick's law, that involves the diffusivity coefficient in the cell membrane of each species. The variation with temperature of these coefficients was taken into account with Arrhenius-like dependence:

$$k_{j,n} = k_j e^{-\frac{E_a}{KT_n}} \tag{8}$$

where k_j are reference diffusion coefficients of the species V_j (with j = *II*, *III*, *IV*, *V*) and E_a is the activation energy (Tab. 2). As the vanadium ions permeate through the membrane and reach the other compartment, they react as reported in [46]; in particular the V^{3+} and V^{2+} ions arriving at the positive compartment, react with VO_2^+:

$$V^{2+} + 2VO_2^+ + 2H^+ \rightarrow 3VO^{2+} + H_2O \tag{9}$$

$$V^{3+} + VO_2^+ \rightarrow 2VO^{2+} \tag{10}$$

While the VO^{2+} and VO_2^+ ions arriving at the negative compartment react with V^{2+}:

$$VO^{2+} + V^{2+} + 2H^+ \rightarrow 2V^{3+} + H_2O \tag{11}$$

$$VO_2^+ + 2V^{2+} + 4H^+ \rightarrow 3V^{3+} + 2H_2O \tag{12}$$

These exothermic reactions occur without electric energy generation, and result in crossover energy losses [47–49]. By combining the species permeation equations and the reactions (9–12), the mass balance equations were derived. The complete description and validation of the crossover model is reported in [16]. As a result of crossover, the vanadium species permeating through the membrane at a rate dM_j/dt reduce the reacting moles available in the proper compartments. Since V^{2+} presents the highest crossover rate, it drives the battery energy reduction rate, that was expressed as:

$$P_{co} = -\Delta G \frac{dM_{II}}{dt} = z\,F\,E_0 \frac{A}{d} \sum_{n=1}^{N} \left(k_{II,n} C_{II,n-} - 2k_{V,n} C_{V,n+} - 2k_{IV,n} C_{IV,n+} \right) \tag{13}$$

where $\Delta G = -zFE_0$, is the total Gibbs reaction energy, with E_0 the cell Nernst potential and $z = 1$ stated the number of charges involved in the electrochemical reactions [50].

Crossover also consists of water dragged by protons constituting the electric current through the membrane. The overall crossover effect is a change of volume in the tanks: the positive electrolyte volume decreases and the negative electrolyte volume increases during charge, and vice versa during discharge. The net effect in a charge/discharge cycle is that the volume of the positive electrolyte increases and the volume of the negative electrolyte decreases, as reported in [51]. During experiments on IS-VRFB, we observed a volume changes of up to 4 L in each charge/discharge cycle.

Tab. 2. Parameters and physical constants used in the numerical models.

Symbol	Parameter /constant	value
A	membrane active area	600 cm^2
C	vanadium concentration	1.6 $mol\,L^{-1}$
C_{sa}	sulfuric acid concentration	4.5 $mol\,L^{-1}$

d	membrane thickness	50 μm
D	pipe diameter	27 mm
E_a	activation energy of electrolyte diffusivity	17340 J mol^{-1}
k_{II}	reference diffusivity of V^{2+} in Nafion 212 [47]	5.76 ×10^{-3} cm^2min^{-1}
k_{III}	reference diffusivity of V^{3+} in Nafion 212 [47]	2.1 ×10^{-3} cm^2min^{-1}
k_{IV}	reference diffusivity of VO^{2+} in Nafion 212 [47]	6.26 ×10^{-3} cm^2min^{-1}
k_V	reference diffusivity of VO_2^+ in Nafion 212 [47]	3.84 ×10^{-3} cm^2min^{-1}
l_{pi}	total length of straight pipes	3.96 m
N	number of cells in the stack	40
V_c	electrolyte volume in each cell	0.4968 L
V_t	tank volume	550 L
μ_+	positive electrolyte average dynamic viscosity	0.007 kg m^{-1}s^{-1}
μ_-	negative electrolyte average dynamic viscosity	0.0055 kg m^{-1}s^{-1}
ρ_+	positive electrolyte average density	1350 kg m^{-3}
ρ_-	negative electrolyte average density	1350 kg m^{-3}
σ_{II}	conductivity of V^{2+}	27.5 S m^{-1}
σ_{III}	conductivity of V^{3+}	17.5 S m^{-1}
σ_{IV}	conductivity of VO^{2+}	27.5 S m^{-1}
σ_V	conductivity of VO_2^+	41.3 S m^{-1}

3.4 Model validations

The validations of the shunt current and crossover models are provided in previously published papers [30] and [16] as already stated. As regards the hydraulic model, it must be pointed out that the pump manufacturer provides only few data for such a small pump model, namely the characteristic head as a function of the flow rate only at the 50 Hz nominal feeding frequency, and the pumps reach only one point of those curves when operated in a given circuit at a fixed frequency. Conversely, the IS-VRFB pumps are operated at variable frequency from 10 to 50 Hz in order to modulate the electrolyte flow rates. Consequently, only one point in this operation range could be compared with the manufacturer date sheet. In addition, the intrinsic accuracy of the computation could hardly exceed few percent when carried out with a conventional hydraulic model as that used in this study (which corresponds to the good practice of hydraulic engineering). Given these constraints, the hydraulic circuit model was validated by considering the pump head value $\Delta p_{h-} = 0.45$ bar indicated in the data sheet at a flow rate $Q = 29.5$ L min^{-1} (violet points in Fig. 4a and Fig. 4b). At this same flow rate, the measured stack pressure drop in the negative electrolyte was $\Delta p_{s-} = 0.28$ bar. From the previous data, the piping pressure drop was derived as $\Delta p_{pi-} = \Delta p_{h-} - \Delta p_{s-} = 0.17$ bar and this value was compared with the model results. At the same $Q = 29.5$ L min^{-1}, the hydraulic model gave a pressure drop in the negative electrolyte piping $\Delta p_{pi-} = 0.19$ bar, with an error of 0.02 bar, that was sufficiently small for the aim of the analysis. A validation in the positive electrolyte piping provided very similar results.

Fig. 4b shows the negative circuit total pressure drop Δp_{h-} and its contributions in the stack Δp_{s-} and in the piping Δp_{pi-}. The former provides the major contribution even in the case of the complex IS-VFRB piping geometry. However, the relative contribution of Δp_{pi-} with respect to Δp_{s-} increases at higher flow rates, because a turbulent regime occurs in the piping earlier than in the stack, where it remains laminar longer. The pressure drop Δp_{s-} never reduces below 58% of the total Δp_{h-}. This result is consistent with data reported in the literature, which indicate that porous electrodes and cell flow channels inside the stack are responsible for pressure drops much larger than those in external piping. For instance, 70% of the whole hydraulic losses occurring in the porous electrode were reported in [35]. In the case of industrial designs with minimized piping lengths, the Δp_s relative contribution is expected to be higher.

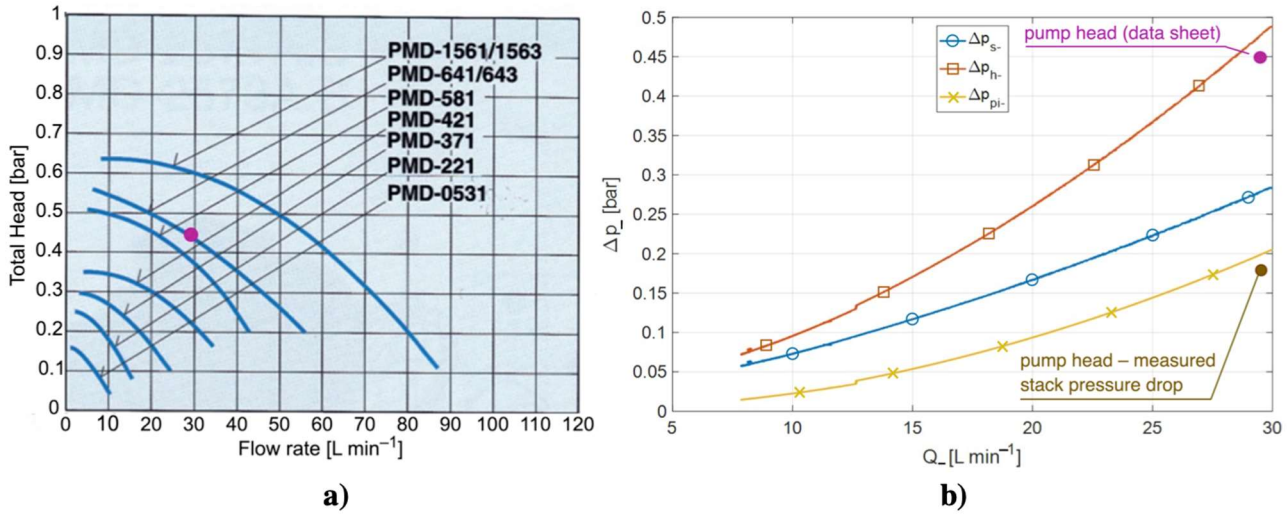

Fig. 4. a) Pump characteristic curve by the manufacturer (Sanso PMD 641); b) Pressure drop profiles in the negative electrolyte circuit vs. flow rate Q at $SOC = 50\%$ (the positive electrolyte piping pressure has a similar profile.) Violet dots identify the same pump working condition and the brown dot the derived piping pressure drop that was used for validation the hydraulic model, i.e. Δp_{pi} of the yellow line.

4. Result analyses

The measured and model-computed losses terms were used to assess the performance of the IS-VRFB facility, in the conceptual framework of the Sankey diagram of Fig. 5, that provides a quick grasp of how the different losses terms impact on the energy efficiency, showing, in particular, that the pumping power P_w was independently supplied, as often happens in flow batteries of this kind.

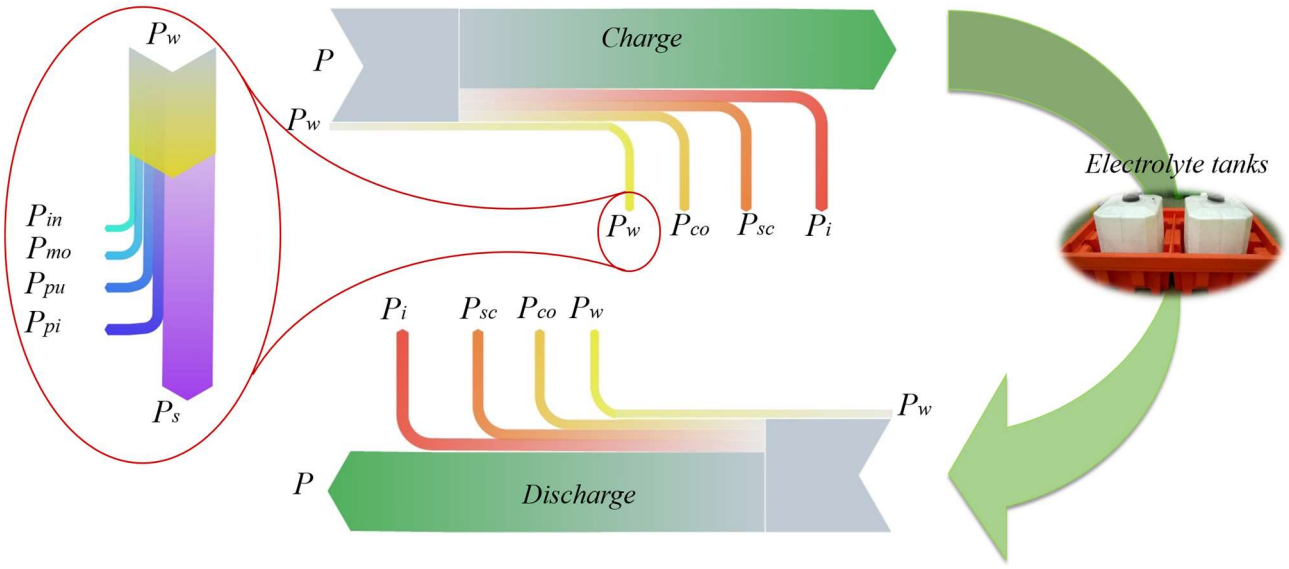

Fig. 5. Sankey diagram of the power flows and loss terms which impact on the energy flows and on the energy efficiency.

4.1 Hydraulic losses analyses

Fig.6 shows the pressure drop in the negative piping Δp_{pi-} as a function of Q. The pie diagrams present the relative contributions to Δp_{pi-} of the different effects at 10 L min^{-1} (i.e. at a specific flow rate of $6.9 \cdot 10^{-3}$ cm s^{-1}) and 29.5 L min^{-1} ($20.5 \cdot 10^{-3}$ cm s^{-1}). Similar values were obtained for the positive electrolyte.

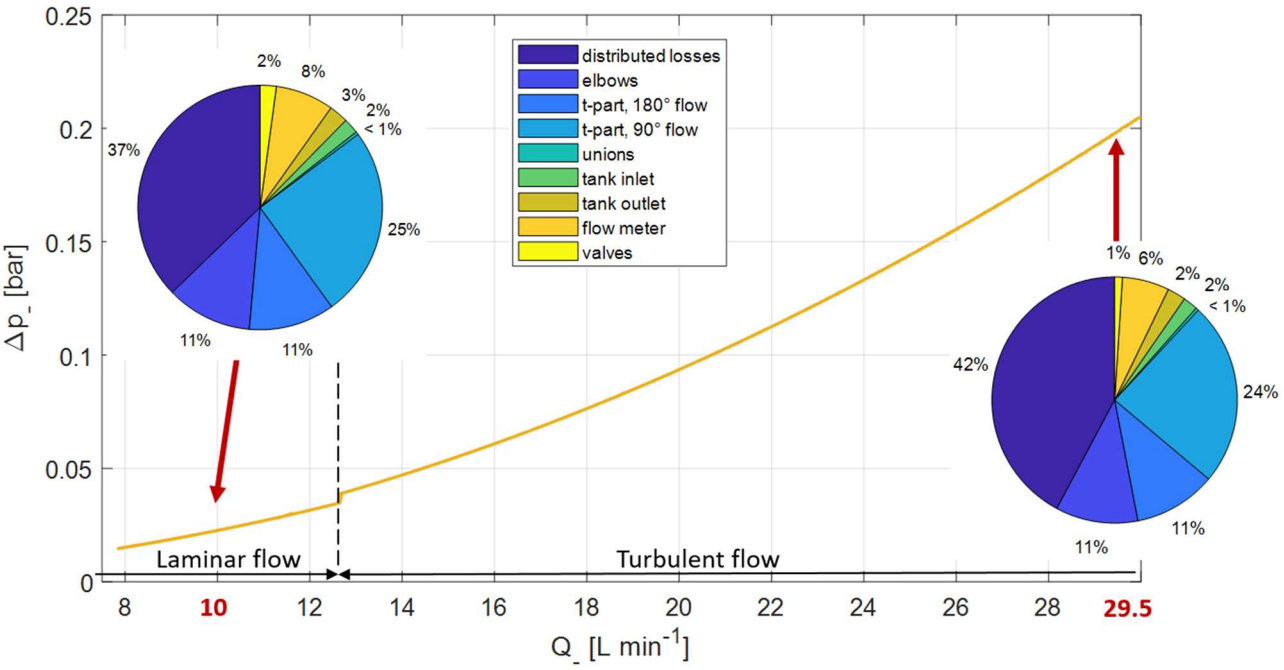

Fig. 6. Negative electrolyte piping pressure drop profile vs. flow rate with pie chart of its contribution in laminar and turbulent flow at SOC = 50% (the positive electrolyte piping pressure has a similar profile.)

Fig.6 shows that the transition from the laminar to the turbulent flow in the piping occurs at Q = 12.8 L min^{-1}. In all cases the concentrated pressure drop $\Delta p_{cn\pm}$ in the local elements of the hydraulic circuit

has a major effect on the total piping pressure drop $\Delta p_{pi\pm}$: it amounts at 63% at 10 L min^{-1} and to 58% at 29.5 L min^{-1}, the remaining being ascribed to the distributed term $\Delta p_{di\pm}$. The 90° T-joints give a higher contribution (25% and 24%) than the 180° T-joints and elbows, because the latter present a smoother curvature. Approximately 7% of the pressure drops occur in the flow meters, due to their reduced internal cross-section. As already noted, the piping pressure drops $\Delta p_{pi\pm}$ and their contributions are expected to be lower in an industrial design, because the piping of the IS-VRFB facility is fully instrumented and designed for a high accessibility and flexible operation, resulting in increased layout complexity and pressure drops.

Fig. 7 shows the hydraulic power losses P_h and their contributions P_{pi} and P_s together with the power losses P_w measured by the wattmeter (Fig. 2a), summed up for the positive and negative circuits as functions of the flow rate Q at SOC = 50%. These profiles, which are similar to those published in [35], highlights the low impact of the net hydraulic power losses compared to the ancillary devices, namely inverters, electric motors and impellers, which, due to their relatively small sizes, are responsible together for 72% of the total losses at Q = 29.5 L min^{-1}, and of an even larger portion at lower flow rates.

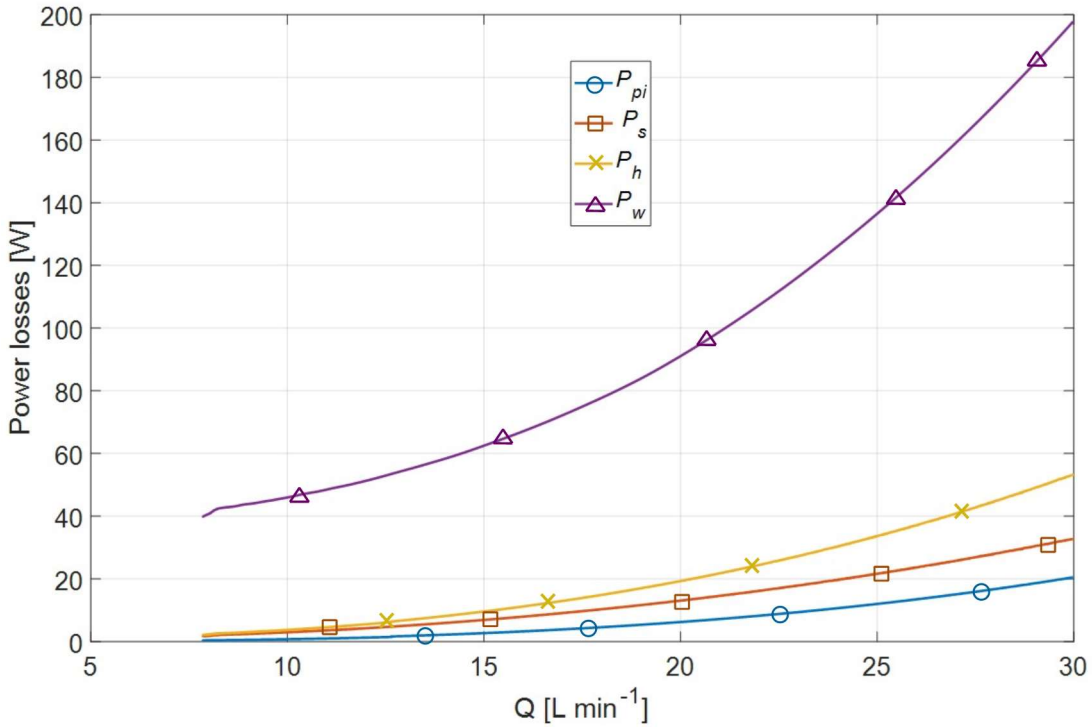

Fig. 7. Profiles of power losses for electrolyte circulation vs. flow rate at SOC = 50% in both positive and negative compartments. The difference between the total value P_w measured by the wattmeter and the hydraulic circuit losses $P_h = P_s + P_{pi}$ is due to P_w in the pump impeller, electric motor and electronic inverter.

4.2 Losses comparison in charge/discharge cycles

The battery losses have been analyzed in charge/discharge round-trip operations at different current levels. A useful parameter driving these cycles is the flow factor, that expresses the ratio between the flow rate of the electric charges moving in the stack with the electrolytes and the electric current generated in the cells from the electrochemical reactions [22]:

$$\alpha = \begin{cases} \dfrac{Q\,F\,C(1-SOC)}{N\,i} & \text{charge} \\ \dfrac{Q\,F\,CSOC}{N\,i} & \text{discharge} \end{cases} \tag{14}$$

where F is the Faraday constant, C is the total vanadium concentration and N is the number of cells in the stack. Experiments were performed at stack currents of 30 A, 50 A and 70 A while the flow factor was kept constant at $\alpha = 8$. This figure is close to the value of 7.5 reported as an optimal value in a study carried out on a 40-cell stack by Tang et al. [52]. Round-trip cycles were performed in the *SOC* ranges shown in Tab. 3, whose limits were chosen for avoiding any dangerous cell condition, mainly resulting from pump constraints. The battery loss contributions in these charge/discharge cycles are shown in Tab. 3. Among the reported values, measurements provided the electric energy supplied to the stack in charge W_{ch}, the electric energy released from the stack in discharge W_{dc} and the total hydraulic energy demand W_{w-rt} in the whole cycles, measured by the wattmeter. Instead, the models provided the round-trip energy losses due to: cell internal overpotentials W_{i-rt}, shunt currents W_{sc-rt} and species crossover W_{co-rt}.

Tab. 3. Numerical and experimental energy terms and system efficiencies during charge/discharge cycles. τ_{rt} = duration of round-trip cycles, W_{ch} = converted electric energy in charge, W_{dc} = converted electric energy in discharge, W_{w-rt} = round-trip total hydraulic losses (i.e. for electrolyte circulation), W_{i-rt} = round-trip losses due to cell internal overpotentials, W_{sc-rt} = round-trip losses due to shunt currents, W_{co-rt} = round-trip losses due to species crossover. * = obtained by time integration of experimental data ** = obtained by time integration of model data.

I [A]	***SOC* range** [%]	τ_{rt} [h]	W_{ch} * [Wh]	W_{dc} * [Wh]	W_{w-rt}* [Wh]	W_{i-rt} ** [Wh]	W_{sc-rt} ** [Wh]	W_{co-rt} ** [Wh]
30	13.1 – 87	19.2	17941	13610	1205	1991	2049	2771
50	19.9 – 78.5	8.7	14273	10165	717	2473	985	1340
70	28.0 – 72.7	4.65	10809	7133	492	2406	515	699

The comparison among these values are more evident in the bar and pie diagrams of Fig. 8. The pie diagrams show that the contributions to the total hydraulic losses W_w did not present significant differences in the three cases at different stack currents. The hydraulic losses in the stack and piping account for 10%–12% of the overall hydraulic losses, whereas a large part of the hydraulic losses was due to inverters, electric motors and impellers, namely ancillaries which do not depend on the design of stack and hydraulic circuits. The two small electric motors were always responsible for almost half of the losses (48%), followed by the impellers (≈37%).

This evidence highlights that high-efficiency devices (pumps, electric motors and inverters) can contribute significantly to the overall system efficiency.

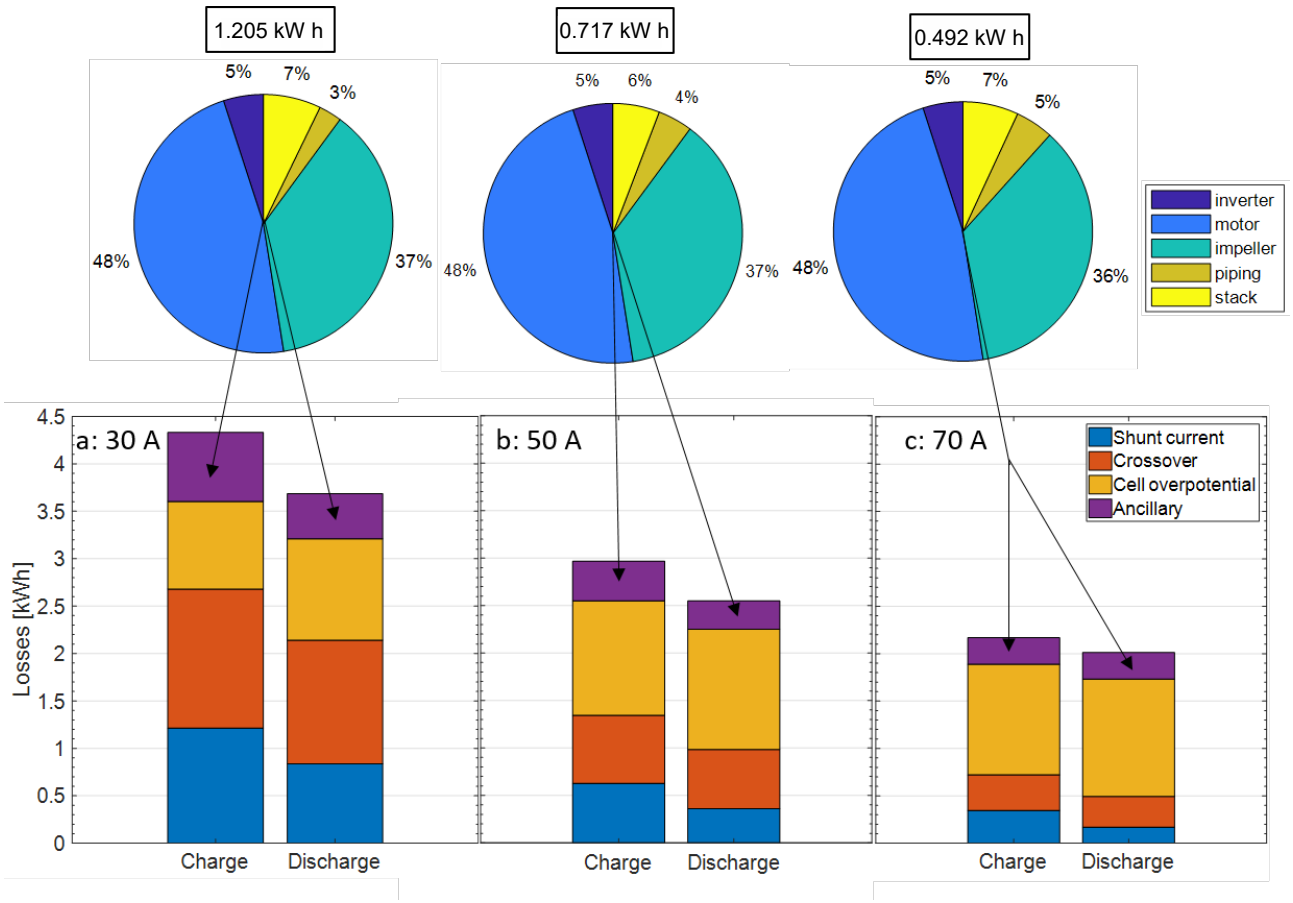

Fig. 8. Battery energy losses contributions in charge/discharge cycles performed at stack currents of: a) 30 A, b) 50 A, c) 70 A in the *SOC* ranges shown in Tab 3. The bar diagrams account for all loss terms, whereas the pie diagrams show the sharing of the hydraulic losses among their contributions.

In addition, the bar diagrams show that the total hydraulic losses W_w were more important when charge/discharge cycles were performed at low-current: W_w was 1.205 kW h in the round-trip operation at 30 A, that is more than twice the value at 70 A. This effect is due to the longer duration of the operation and to the low pump efficiency η_{pu} at low flow rate (Fig. 2a). The losses due to shunt currents and crossover were also observed to increase with decreasing stack current, due to the longer duration of the operation (Fig. 8). It must be noted that shunt current losses must also be taken into account duly, although some studies claim that they do not affect markedly the electrical performance of a VRFB, being two order of magnitude lower than the nominal stack current, as reported by Zang et al. [34] and Bhattacharjee et al. [53]. Conversely, our results show that in a compact VRFB stack they have an influence comparable to other losses, especially at low load. In particular, we found shunt-current losses greater than the total hydraulic losses in the 30 A and 50 A operations. In addition, combining the percentage of the pie diagrams with the total hydraulic losses value of Tab. 3, it can be found that the stack hydraulic losses W_s are 4.1% (84 W h out of 2.049 kW h), 4.3% (43 W h out of 985 W h) and 6.7% (34.4 W h out of 985 W h) with respect to the shunt current losses W_{sc} in charge-

discharge cycles at 30 A, 50 A and 70 A, respectively. These results highlight that shunt currents can significantly affect the efficiency of an industrial VRFB.

4.3 Energy efficiencies

A number of efficiency indicators are proposed in the literature for assessing the performance of VRFBs: voltage efficiency [52], coulombic efficiency and current efficiency [54]. The round-trip efficiency (*RTE*) is a figure of merit that summarizes the others and is presented in the literature in different forms. A common definition, also dubbed energy efficiency (*EE*), consists of the ratio between the energy released from the stack during discharge with respect to the energy released to the stack during charge: $EE = \int \tau_{dc} P\, dt \,/\, \int \tau_{ch} P\, dt = W_{dc}/W_{ch}$. In this expression, the energies converted by the stack account for the loss terms due to overpotentials W_i, shunt currents W_{sc}, and species crossover W_{co}. This figure can be convenient for qualifying a single cell, but can be less significant if referred to a stack, because it neglects the pumping power W_w, when independently supplied. A more comprehensive definition of the efficiency suitable for stacks, sometimes dubbed system efficiency (*SE*), was used in our analyses, that includes the energy demand from the hydraulic circuit [54]:

$$SE = \frac{\int_{\tau_{dc}} P - P_w dt}{\int_{\tau_{ch}} P + P_w dt} = \frac{W_{dc} - W_w}{W_{ch} + W_w} \tag{15}$$

The values of this *SE*, obtained for measurements of the stack and pumps powers according to (15) are reported in Tab. 4. The table shows also the SE_{mod} efficiency values computed with the following expression that uses the numerical data provided by the models:

$$SE_{mod} = \frac{W_{ch} - W_{i-rt} - W_{sc-rt} - W_{co-rt} - W_{w-dc}}{W_{ch} + W_{w-ch}} \tag{16}$$

Tab. 4. System efficiency figures obtained from energy measurements and computations. τ_{rt} = duration of round-trip cycles, *SE* = system efficiency computed by using measurements in (15), SE_{mod} = system efficiency based on model data used in (16), ε = discrepancy between *SE* and SE_{mod} values.

I [A]	***SOC* range** [%]	τ_{rt} [h]	***SE*** [%]	SE_{mod} [%]	ε [%]
30	13.1 – 87	19.2	70.35	70.72	+0.53
50	19.9 – 78.5	8.7	67.10	66.67	–0.64
70	28.0 – 72.7	4.65	62.42	62.81	+0.62

As indicated in Tab. 4, the relative errors between the two set of *SE* and SE_{mod} values were always lower than 1%, which provided a further validation of the model reliability. In addition, the *SE* values presented in the table are in agreement with the efficiencies reported in the literature for kW-class VRFB systems [55,56].

5. Conclusions

The losses and efficiency analysis here proposed provides results which, strictly speaking, hold for the IS-VRFB system on which they have been measured and computed. Nevertheless, some general considerations can be drawn which apply also to any other large industrial-scale VRFB system. Firstly, the design of a compact VRFB stack provided with a quite large number of cells should be addressed to reduce shunt currents, by increasing the electrolyte electric resistances in the internal manifolds and flow channels, with marginal consequences on the hydraulic performance. In other words, longer and thinner flow paths should be preferred in the trade-off between shunt current and hydraulic losses, in the limit that flow channels do not risk to be clogged by electrolyte impurities. For example, the flow channels of the flow frame (e.g. those represented in [36]) could be lengthened without significant effects on the hydraulic losses.

Secondly, at high-current operations the cell overpotential losses are larger than crossover losses. Consequently, the cell internal equivalent resistances (which are mainly due to the membrane ohmic overpotentials as reported in [22]), impacts on the efficiency more than the membrane species permeability from which the crossover losses originate, particularly in a compact VRFB stack with a smaller cell active area capable of operating at higher current density than those usually reported in the literature (e.g. the 19-cell stack with 1500 cm^2 area of the 2.5 kW/15kWh reported by Tang et al. [33]). As a matter of fact, in our study crossover losses were a little higher than the overpotential losses only in the 30 A operation (Tab. 3). Consequently, increasing the membrane ion conductivity is a more important issue than reducing its vanadium species permeability, especially in a high current operation. In addition, since the effect of the relatively thick electrodes (5.7 mm) of IS-VRFB on the cell internal resistance was not negligible, a reduction of the internal losses can also be achieved with thinner electrodes provided with high reaction activity.

Thirdly, hydraulic losses were found to depend largely on the low efficiency of the electric motors and of the pumps as typically occur in small size devices (e.g. 50% and 20%–55%, respectively, in our study). Conversely, we found that only less than a quarter of overall hydraulic losses were due to the hydraulic circuit, i.e. to stack and piping. It must be noted, however, that ancillary device efficiencies can be much higher in larger units fitted to larger systems. For instance, a 5-kW motor suitable for a 150-kW VRFB can have an efficiency above 75% and larger motors can easily exceed 90%. At the best of our knowledge, similar analyses of the effect of ancillary losses were largely overlooked in the existing literature.

6. Acknowledgements

This work was funded by the University of Padua within the Project 2016 of the Interdepartmental Centre Giorgio Levi Cases for Energy Economics and Technology “Next-Generation VRFB Energy Storage Systems” (GUAR_RICERCALASCITOLEVI17_02).

References

[1] Alotto P, Guarnieri M, Moro F. Redox flow batteries for the storage of renewable energy: A review. Renew Sustain Energy Rev 2014; 29: 325–355; doi:10.1016/j.rser.2013.08.001.

[2] Li X, Zhang H, Mai Z, Zhang H, Vankelecom I. Ion exchange membranes for vanadium redox flow battery (VRB) applications. Energy Environ Sci 2011; 4: 1147–1160; doi:10.1039/c0ee00770f.

[3] Kear G, Shah A.A, Walsh F.C. Development of the all-vanadium redox flow battery for energy storage: A review of technological, Financial and policy aspects. Int J Energy Res 2012. 36: 1105–1120; doi:10.1002/er.1863.

[4] Rydh C.J. Environmental assessment of vanadium redox and lead-acid batteries for stationary energy storage. J Power Sources 1999; 80: 21–29; doi:10.1016/S0378-7753(98)00249-3.

[5] Khazaeli A, Vatani A, Tahouni N, Panjeshahi M.H. Numerical investigation and thermodynamic analysis of the effect of electrolyte flow rate on performance of all vanadium redox flow batteries. J Power Sources 2015; 293: 599–612; doi:10.1016/j.jpowsour.2015.05.100.

[6] Maggiolo D, Zanini F, Picano F, Trovò A, Carmignato S, Guarnieri M. Particle based method and X-ray computed tomography for pore-scale flow characterization in VRFB electrodes. Energy Storage Materials 2019; 16: 91-96, doi: 10.1016/j.ensm.2018.04.021.

[7] Di Blasi A, Briguglio N, Di Blasi O, Antonucci V. Charge-discharge performance of carbon fiber-based electrodes in single cell and short stack for vanadium redox flow battery. Appl Energy 2014; 125: 114–122; doi:10.1016/j.apenergy.2014.03.043.

[8] Mazúr P, Mrlík J, Beneš J, Pocedič J, Vrána J, Dundálek J, Kosek J. Performance evaluation of thermally treated graphite felt electrodes for vanadium redox flow battery and their four-point single cell characterization. J Power Sources 2018; 380: 105–114; doi:10.1016/j.jpowsour.2018.01.079.

[9] Chen D, Chen X, Ding L, Li X. Advanced acid-base blend ion exchange membranes with high performance for vanadium flow battery application. J Memb Sci 2018; 553: 25–31; doi:10.1016/j.memsci.2018.02.039.

[10] Kim J, Lee Y, Jeon J.D, Kwak S.Y. Ion-exchange composite membranes pore-filled with sulfonated poly(ether ether ketone) and Engelhard titanosilicate-10 for improved performance of vanadium redox flow batteries. J Power Sources 2018; 383: 1–9; doi:10.1016/j.jpowsour.2018.02.028.

[11] Lei Y, Zhang B.W, Zhang Z.H, Bai B.F, Zhao T.S. An improved model of ion selective adsorption in membrane and its application in vanadium redox flow batteries. Appl Energy 2018; 215: 591–601; doi:10.1016/j.apenergy.2018.02.042.

[12] Cao L, Skyllas-Kazacos M, Menictas C, Noack J. A review of electrolyte additives and impurities in vanadium redox flow batteries. J Energy Chem 2018; 27(5): 1269–1291; doi:10.1016/j.jechem.2018.04.007.

[13] Vijayakumar M, Li L, Graff G, Liu W.J, Zhang H, Yang Z, Hu J.Z. Towards understanding the poor thermal stability of V5+electrolyte solution in Vanadium Redox Flow Batteries. J Power Sources 2011; 196: 3669–3672; doi:10.1016/j.jpowsour.2010.11.126.

[14] Roe S, Menictas C, Skyllas-Kazacos M. A High Energy Density Vanadium Redox Flow Battery with 3 M Vanadium Electrolyte. J Electrochem Soc 2016; 163: A5023–A5028; doi:10.1149/2.0041601jes.

[15] Arenas L.F, Ponce de León C, Walsh F.C. Engineering aspects of the design, construction and performance of modular redox flow batteries for energy storage. J Energy Storage 2017; 11: 119–153; doi:10.1016/j.est.2017.02.007.

[16] Trovò A, Marini G, Sutto A, Alotto P, Moro F, Giomo M, Guarnieri M. Standby thermal model of a vanadium redox flow battery stack with crossover and shunt-current effects. Appl Energy 2019; 240: 893-906; doi: 10.1016/j.apenergy.2019.02.067.

[17] Pugach M, Kondratenko M, Briola S, Bischi A. Zero dimensional dynamic model of vanadium redox flow battery cell incorporating all modes of vanadium ions crossover. Appl. Energ. 2018; 226: 560-569: doi: 10.1016/j.apenergy.2018.05.124 .

[18] Ye Q, Hu J, Cheng P, Ma Z. Design trade-offs among shunt current, pumping loss and compactness in the piping system of a multi-stack vanadium flow battery. J Power Sources 2015; 296: 352–364; doi:10.1016/j.jpowsour.2015.06.138.

[19] Darling R.M, Perry M.L. The Influence of Electrode and Channel Configurations on Flow Battery Performance. J Electrochem Soc 2014; 161: A1381–A1387; doi:10.1149/2.0941409jes.

[20] Zheng Q, Xing F, Li X, Ning G, Zhang H. Flow field design and optimization based on the mass transport polarization regulation in a flow-through type vanadium flow battery. J Power Sources 2016; 324: 402–411; doi:10.1016/j.jpowsour.2016.05.110.

[21] Xu Q, Zhao T.S, Zhang C. Performance of a vanadium redox flow battery with and without flow fields. Electrochim Acta 2014; 142: 61-67; doi:10.1016/j.electacta.2014.07.059.

[22] Trovò A, Picano F, Guarnieri M. Maximizing Vanadium Redox Flow Battery Efficiency: Strategies of Flow Rate Control. IEEE Int. Symp. Ind Electron 2019, 8781152: 1977-1982; doi: 10.1109/ISIE.2019.8781152.

[23] Xiong B, Zhao J, Tseng K.J, Skyllas-Kazacos M, Lim T.M, Zhang Y. Thermal hydraulic behavior and efficiency analysis of an all-vanadium redox flow battery. J Power Sources 2013; 242: 314–324; doi:10.1016/j.jpowsour.2013.05.092.

[24] Wang T, Fu J, Zheng M, Yu Z. Dynamic control strategy for the electrolyte flow rate of vanadium redox flow batteries. Appl Energy 2018; 227: 613–623; doi:10.1016/j.apenergy.2017.07.065.

[25] Wei Z, Zhao J, Skyllas-Kazacos M, Xiong B. Dynamic thermal-hydraulic modeling and stack flow pattern analysis for all-vanadium redox flow battery. J Power Sources 2014; 260: 89–99; doi:10.1016/j.jpowsour.2014.02.108.

[26] Xing F, Zhang H, Ma X. Shunt current loss of the vanadium redox flow battery. J Power Sources 2011; 196: 10753–10757. doi:10.1016/j.jpowsour.2011.08.033.

[27] Schaeffer J.A, Chen L Der, Seaba J.P. Shunt current calculation of fuel cell stack using Simulink®. J Power Sources 2008; 182: 599–602; doi:10.1016/j.jpowsour.2008.04.014.

[28] Chen Y-S, Ho S-Y, Chou H-W, Wei H-J. Modeling the effect of shunt current on the charge transfer efficiency of an all-vanadium redox flow battery. J Power Sources 2018; 390: 168–175; doi.org/10.1016/j.jpowsour.2018.04.042.

[29] Fink H, Remy M. Shunt currents in vanadium flow batteries: Measurement, modelling and implications for efficiency. J Power Sources 2015; 284: 547–553; doi:10.1016/j.jpowsour.2015.03.057.

[30] Trovò A, Saccardo A, Giomo M, Guarnieri M. Thermal modeling of industrial-scale vanadium redox flow batteries in high-current operations. J Power Sources 2019; 424: 204-214; doi.org/10.1016/j.jpowsour.2019.03.080.

[31] Wandschneider F.T, Röhm S, Fischer P, Pinkwart K, Tübke J, Nirschl H. A multi-stack simulation of shunt currents in vanadium redox flow batteries. J Power Sources 2014; 261: 64–74; doi:10.1016/j.jpowsour.2014.03.054.

[32] Moro F, Trovò A, Bortolin S, Del Col D, Guarnieri M. An alternative low-loss stack topology for vanadium redox flow battery: Comparative assessment. J Power Sources 2017; 340: 229–241; doi:10.1016/j.jpowsour.2016.11.042.

[33] Tang A, Mc Cann J, Bao J, Skyllas-Kazacos M. Investigation of the effect of shunt current on battery efficiency and stack temperature in vanadium redox flow battery. J Power Sources 2013; 242: 349–356; doi:10.1016/j.jpowsour.2013.05.079.

[34] Zhang Y, Zhao J, Wang P, Skyllas-Kazacos M, Xiong B, Badrinarayanan R. A comprehensive equivalent circuit model of all-vanadium redox flow battery for power system analysis. J Power Sources 2015; 290: 14–24. doi:10.1016/j.jpowsour.2015.04.169.

[35] Kim S, Thomsen E, Xia G, Nie Z, Bao J, Recknagle K, Wang W, Viswanathan V, Luo Q, Wei X, Crawford A, Coffey G, Maupin G, Sprenkle V. 1 kW/1 kWh advanced vanadium redox flow battery utilizing mixed acid electrolytes. J Power Sources 2013; 237: 300–309; doi:10.1016/j.jpowsour.2013.02.045.

[36] Guarnieri M, Trovò A, D'Anzi A, Alotto P. Developing vanadium redox flow technology on a 9-kW 26-kWh industrial scale test facility: Design review and early experiments. Appl Energy 2018; 230: 1425-1434; doi:10.1016/j.apenergy.2018.09.021.

[37] Guarnieri M, Trovò A, Marini G, Sutto A, Alotto P. High current polarization tests on a 9 kW vanadium redox flow battery J Power Sources 2019; 431: 239-249; doi.org/10.1016/j.jpowsour.2019.05.035.

[38] Wei Z, Lim T.M, Skyllas-Kazacos M, Wai N, Tseng K.J. Online state of charge and model parameter co-estimation based on a novel multi-timescale estimator for vanadium redox flow battery. Appl Energy 2016; 172: 169-179; doi.org/10.1016/j.apenergy.2016.03.103.

[39] Wei Z, Zhao J, Ji D, Tseng K.J. A multi-timescale estimator for battery state of charge and capacity dual estimation based on an online identified model. Appl Energy 2017; 204: 1264-1274; doi.org/10.1016/j.apenergy.2017.02.016

[40] Li Y, Zhang X, Bao J, Skyllas-Kazacos M. Studies on optimal charging conditions for vanadium redox flow batteries. J Energy Storage 2017; 11: 191–199; doi:10.1016/j.est.2017.02.008.

[41] Blanc C, Rufer A. Multiphysics and energetic modeling of a vanadium redox flow battery. 2008 IEEE Int. Conf. Sustain. Energy Technol. ICSET 2008, 2008; 978-1-4244-1888-6/08/$25; doi:10.1109/ICSET.2008.4747096.

[42] Munson BR, Okiishi T.H, Huebsch W.W, Rothmayer A.P. Fundamentals of fluid mechanic. New York, NY: John Wiley & Sons, 2012.

[43] ASV Stübbe GmbH & Co. KG, "Kugelhahn C200," www.asv-stuebbe.de.

[44] Mohamed M.R, Ahmad H, Seman M.N.A, Razali S, Najib MS. Electrical circuit model of a vanadium redox flow battery using extended Kalman filter. J Power Sources 2013; 239: 284–293; doi:10.1016/j.jpowsour.2013.03.127.

[45] Tang A, Bao J, Skyllas-Kazacos M. Dynamic modelling of the effects of ion diffusion and side reactions on the capacity loss for vanadium redox flow battery. J Power Sources 2011; 196: 10737–10747; doi:10.1016/j.jpowsour.2011.09.003.

[46] Tang A, Bao J, Skyllas-Kazacos M. Thermal modelling of battery configuration and self-discharge reactions in vanadium redox flow battery. J Power Sources 2012; 216: 489–501;doi:10.1016/j.jpowsour.2012.06.052.

[47] Yan Y, Li Y, Skyllas-Kazacos M, Bao J. Modelling and simulation of thermal behaviour of vanadium redox flow battery; J Power Sources 2016; 322: 116–128; doi:10.1016/j.jpowsour.2016.05.011.

[48] Li Y, Skyllas-Kazacos M, Bao J. A dynamic plug flow reactor model for a vanadium redox flow battery cell. J Power Sources 2016; 311: 57–67; doi:10.1016/j.jpowsour.2016.02.018.

[49] Oh K, Won S, Ju H. A comparative study of species migration and diffusion mechanisms in all-vanadium redox flow batteries. Electrochim Acta 2015; 181: 238–247; doi:10.1016/j.electacta.2015.03.012.

[50] Pavelka M, Wandschneider F, Mazur P. Thermodynamic derivation of open circuit voltage in vanadium redox flow batteries. J Power Sources 2015; 293: 400–408; doi:10.1016/j.jpowsour.2015.05.049.

[51] Sun C, Chen J, Zhang H, Han H, Luo K. Investigations on transfer of water and vanadium ions across

Nafion membrane in an operating vanadium redox flow battery. J Power Sources 2010; 195(3): 890-897; doi: 10.1016/j.jpowsour.2009.08.041.

[52] Tang A, Bao J, Skyllas-Kazacos M. Studies on pressure losses and flow rate optimization in vanadium redox flow battery. J Power Sources 2014; 248: 154–62; doi:10.1016/j.jpowsour.2013.09.071.

[53] Bhattacharjee A, Saha H. Design and experimental validation of a generalised electrical equivalent model of Vanadium Redox Flow Battery for interfacing with renewable energy sources. J Energy Storage 2017; 13: 220–232; doi:10.1016/j.est.2017.07.016.

[54] Yang W.W, Yan F.Y, Qu Z.G, He Y.L. Effect of various strategies of soc-dependent operating current on performance of a vanadium redox flow battery. Electrochim Acta 2018; 259: 772–782 ; doi:10.1016/j.electacta.2017.10.201.

[55] Guarnieri M, Mattavelli P, Petrone G, Spagnuolo G. Vanadium redox flow batteries: Potentials and challenges of an emerging storage technology. IEEE Ind Electron Mag 2016; 10(4): 20–31; doi:10.1109/MIE.2016.2611760.

[56] Guarnieri M, Bovo A, Giovannelli A, Mattavelli P. The VERITAS multi-technology microgrid experiment: a design review. IEEE Ind Electron Mag 2018; 12: 19–31; doi: 10.1109/MIE.2018.2855735.